Journal of Nuclear Materials 577 (2023) 154261

Contents lists available at ScienceDirect

Journal of Nuclear Materials

journal homepage: www.elsevier.com/locate/jnucmat

Ab-initio investigation of mechanical and fracture-related properties of W-Re σ and χ precipitates

Anders Vesti[a,*], Praveenkumar Hiremath[a], Solveig Melin[a], Pär A.T. Olsson[a,b]

[a] Division of Mechanics, Materials & Components, Lund University, Box 118, SE-221 00 Lund, Sweden
[b] Materials Science and Applied Mathematics, Malmö University, SE-205 06 Malmö, Sweden

ARTICLE INFO

Article history:
Received 26 September 2022
Revised 12 December 2022
Accepted 10 January 2023
Available online 13 January 2023

Keywords:
Tungsten
Elastic properties
GSFE
Fracture toughness
Frank-Kasper phases
DFT

ABSTRACT

Tungsten (W) is a leading candidate for plasma-facing materials in fusion reactors. Recently, experiments have shown that during neutron irradiation, W and its transmutation products, mainly rhenium (Re), will form precipitates of the σ and χ types. This study identifies close-packed planes of the σ- and χ-phases in the W-Re system and uses *ab-initio* methods to identify mechanical properties such as elastic constants, generalized stacking fault energies (GSFE), and fracture toughness associated with brittle and ductile mechanisms. By utilizing a sublattice model we demonstrate how these properties depend on the Re content. For Re concentrations in the range where the σ- and χ-phases are stable, we find a weak dependency on the Re content, meaning that the elemental composition has little influence on the mechanical and fracture-related properties.

1. Introduction

Choosing suitable plasma-facing materials (PFMs) is essential for the success of nuclear fusion reactors. This is, however, a non-trivial task since the PFMs must endure extreme environments of high thermal loads, plasma exposure, and intense neutron irradiation [1–4]. In recent years tungsten (W) has emerged as a prime candidate for PFMs – much thanks to its high melting point, high thermal conductivity, and low sputtering yield [5–7]. In light of these attractive features, W has been successfully used in several fusion experimental facilities [7,8] and it will be used as PFM for the divertor in ITER [9,10]. It is also anticipated to play an important role for plasma-facing components in future reactors, such as the planned future class of demonstration power plants (DEMO) [6,11].

Since PFMs will operate in aggressive environments with high neutron radiation exposure, research efforts directed towards elucidating how irradiation damage will affect the mechanical and thermal properties of W have intensified in recent years. The observed microstructural damage associated with irradiation includes the generation of interstitials, vacancies, voids, and dislocations loops, which promote increased brittle-to-ductile transition temperature (DBTT) [12]. Moreover, the generation of transmutation products – mainly rhenium (Re) and osmium (Os) – provides a new set of challenges. Theoretical investigations predict the Re content in the first wall armor of a DEMO-like reactor to reach 3 at.% within five years of operation [11], while the estimated end-of-service concentration in the first wall armor of an ITER-like reactor is 6 at.% Re (3 at.% Os) [13]. When subjected to neutron radiation, the transmutation of W to Re will contribute to radiation-induced precipitation of the topologically close-packed σ- and χ-phases, which promotes a gradual hardening of the material while in operation. Neutron irradiation experiments of W and W-Re alloy samples have demonstrated the precipitation of the σ- and χ-phases for Re concentrations much lower than under equilibrium conditions [14–16]. Recently, Dürrschnabel et al. [17] observed σ and χ precipitates in neutron irradiated W samples containing only 2 – 4 at.% Re. Moreover, Lloyd et al. [18] reported the observation of precipitates with chemical composition consistent with the σ-phase in irradiated samples containing as little as 1.09 – 1.26 at.% Re. *Ab initio* studies based on density functional theory (DFT) have revealed that the formation of precipitates at very low Re concentrations is due to the low energy barrier associated with migration of mixed W-Re dumbbell interstitials [18–23].

To explore the physical and mechanical properties of the σ- and χ-phases in the W-Re system, Berne et al. [24] utilized DFT-based methods to explore the formation energy and site occupancy of the σ-phase. In agreement with neutron-diffraction experiments, they found tendencies of preferential site occupancy for the Re atoms. Likewise, Crivello and Joubert [25] deduced the formation energy

* Corresponding author.
E-mail address: Anders.Vesti@mek.lth.se (A. Vesti).

https://doi.org/10.1016/j.jnucmat.2023.154261

and site occupation for the χ-phase in W-Re, while Bonny et al. [26] expanded on these works by studying elastic constants, bulk modulus, and shear modulus of the σ-phase for different concentrations utilizing the aforementioned site occupations. The latter used their results to create an empirical *embedded atom method* (EAM) potential for classical modelling of the W-Re system [27]. In parallel with these research activities, an additional binary potential was generated by Setyawan et al. [28], relying on formation energies of the σ- and χ-phases obtained from DFT modelling as fitting parameters.

At present, knowledge of important fundamental properties of the σ- and χ-phases, such as the fracture toughness associated with ductile and brittle mechanisms, is missing, along with the elastic constants of the χ-phase. Thus, the objective of the present study is to clarify the impact of crystallography and Re concentration on the fracture mechanical properties of the two phases. To this end, we identify and evaluate energy release rate and generalized stacking fault energy (GSFE) of preferential slip systems and cleavage planes by means of DFT modelling to assess the fracture toughness based on the Griffith and Rice theories [29,30]. This serves two purposes; Most importantly, the herein-acquired knowledge will be used to assess how the fracture mechanical properties vary as the Re content increases over the lifetime of the reactor. Moreover, the herein-generated data can be used to evaluate and generate empirical potentials for modelling crack-tip events.

This paper is outlined as follows. In the next section, we provide a brief background on the crystallography of the σ- and χ-phases. Next, we describe the methods used to estimate their mechanical and fracture-related properties as well as the numerical details of the DFT calculations. In the section thereafter, we present the results of this work followed by a discussion section where the results for the σ- and χ-phases are compared to both simulated and experimental data of pristine W. Finally, the paper concludes with a summary of the work and the key findings.

1.1. The σ- and χ-phases

The σ- and χ-phases are topologically close-packed phases, which belong to the class of non-stoichiometric Frank-Kasper phases [32]. The σ-phase is thermodynamically stable in the concentration range between 30–70 at.% Re, while the χ-phase is stable at higher Re contents, corresponding to 66–90 at.% Re [33]. The σ-phase has tetragonal crystal symmetry, belonging to the space-group $P4_2/mnm$. Its unit cell, shown in Fig. 1(a), contains 30 atoms located at five nonequivalent Wyckoff sites, henceforth referred to as $A-E$ [34]. The χ-phase is a cubic crystal belonging to the $I\bar{4}3m$ space-group. The unit cell, shown in Fig. 1(b), comprises 58 atoms distributed among four Wyckoff sites, $A-D$ [35]. While both phases are non-stoichiometric, complete disorder is not observed either. Previous *ab initio* works suggest that Re preferentially occupies Wyckoff sites with low coordination number, i.e. sites A and D for the σ-phase and sites C and D for the χ-phase [24–26]. Such tendencies have been confirmed experimentally for the case of the σ-phase [24].

2. Method

2.1. Sublattice model

To determine the occupancy of the Wyckoff sites, a sublattice model (see [36]) was constructed and the Gibbs free energy was minimized under the requirement of ideal mixing [25]:

$$G(x_{Re}, T) = G^{ref} - T \cdot S^{mix}, \tag{1}$$

where G^{ref} is a weighted sum of the enthalpies of formation of all possible configurations:

$$\begin{aligned} G^{ref,\sigma} &= \sum_{k,l,m,n,o=W,Re} y_k^A y_l^B y_m^C y_n^D y_o^E H^{\sigma}_{klmno} \\ G^{ref,\chi} &= \sum_{k,l,m,n=W,Re} y_k^A y_l^B y_m^C y_n^D H^{\chi}_{klmn}, \end{aligned} \tag{2}$$

where y_c^s is the site occupancy of Wyckoff site s with element c (W or Re). As indicated by Eq. (2), the σ-phase has five Wyckoff sites $A-E$ whereas χ has four: $A-D$. The enthalpies of formation, $H^{\chi/(\sigma)}$, were calculated by subtracting the total energy per atom, $E^{\chi/(\sigma)}_{klmn(o)}$, and the proportionate amount of W and Re in their reference states:

$$H^{\chi/(\sigma)}_{klmn(o)} = E^{\chi/(\sigma)}_{klmn(o)} - x_W \cdot E^{BCC}_W - x_{Re} \cdot E^{HCP}_{Re}, \tag{3}$$

where x_c is the ratio of element c in the $klmn(o)$ configuration.

The second term in Eq. (1) is the ideal entropy of mixing given by:

$$S^{mix} = \frac{k_B}{N_{cell}} \sum_s m_s \sum_{k=W,Re} y_k^s \ln(y_k^s), \tag{4}$$

where k_B is Boltzmann's constant, N_{cell} number of atoms in the σ or χ unit cells and m_s is the multiplicity of Wyckoff site s.

The preferential site occupancies of Re, y^s_{Re}, were obtained by minimizing Eq. (1) with respect to the y^s_{Re}'s. Choosing the temperature $T = 1500$ K provided a good fit to the experimental data given in [24].

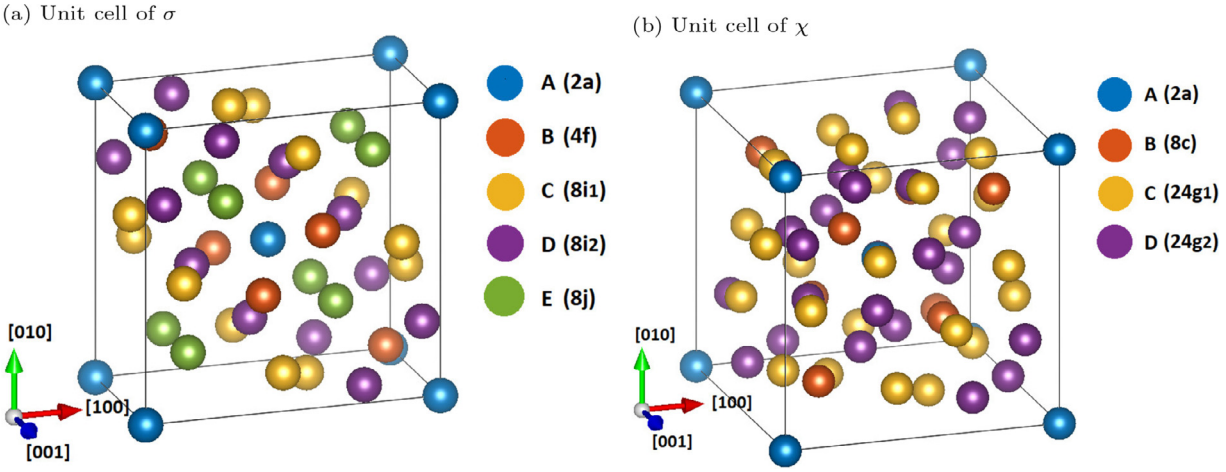

Fig. 1. Unit cells of the (a) σ- and (b) χ-phases. Atomic positions have been colored with respect to their Wyckoff sites. The unit cells are created using VESTA [31].

2.2. Close-packed planes and generalized stacking fault energies

To identify close-packed planes of σ and χ, we adopted the method proposed by Kelly et al. [37]. This approach relies on characterizing the crystal plane packing-density based on the area-per-atom, A_{hkl}, which was approximated as

$$A_{\mathrm{hkl}} = \frac{V}{|F_{\mathrm{hkl}}| \cdot d_{\mathrm{hkl}}}, \tag{5}$$

where V is the unit cell volume, d_{hkl} is the interplanar spacing with hkl being the Miller indices of the plane, and $|F_{\mathrm{hkl}}|$ is the structure factor, given by

$$F_{\mathrm{hkl}} = \sum_{j}^{N} f_j e^{-2\pi i(\mathrm{h}x_j + \mathrm{k}y_j + \mathrm{l}z_j)}, \tag{6}$$

where the sum covers the N atoms in the unit cell, x_j, y_j, z_j are the coordinates of atom j, and the scattering factor f_j was chosen equal to unity for all atoms [37].

For determining the GSFE landscape, a periodic supercell was constructed with one of the periodic boundaries coinciding with the slip plane of interest. Rigid displacements were effectuated by imposing in-plane displacements to the supercell vectors, such that a shearing interface emerged between the neighboring periodic cells. Whenever possible, we fully exploited the symmetry of the slip planes such that only part of the energy landscape had to be probed to produce the full energy landscape. During relaxation, atoms were allowed to relax only in the direction parallel to the slip plane normal.

Owing to the corrugated nature of some of the crystal planes in the Frank-Kasper phases, atoms located on opposite sides of the interface were prior to relaxation occasionally too closely separated to ensure numerical stability. In such cases, the closely positioned atoms were displaced in the normal direction of the slip plane, to increase the initial separation. A convergence test was performed to determine the supercell height, which revealed that the height of 13 Å gave converged results.

Because obtaining a full GSFE surface is computationally expensive, we limited ourselves to the structures of the lowest formation enthalpy in the sublattice model for both phases. By using the full GSFE surfaces, we located the positions of the unstable stacking faults and calculated the unstable stacking fault energies for all the structures in the sublattice model. The unstable stacking fault energy, γ_{us}, as a function of Re content, was calculated as a weighted average using the Wyckoff site occupancies, y_c^s's, as weights:

$$\begin{aligned}\gamma_{us}^{\sigma}(x_{Re}) &= \sum_{k,l,m,n,o} y_k^A y_l^B y_m^C y_n^D y_o^E \gamma_{us}^{\sigma}(k,l,m,n,o),\\ \gamma_{us}^{\chi}(x_{Re}) &= \sum_{k,l,m,n} y_k^A y_l^B y_m^C y_n^D \gamma_{us}^{\chi}(k,l,m,n).\end{aligned} \tag{7}$$

2.3. Elastic constants and fracture toughness

The elastic constants, bulk, and shear moduli of the σ-phase have previously been determined using DFT by Bonny et al. [26]. We confirmed their results and adopted them herein. The cubic χ-phase has three independent elastic constants c_{11}, c_{12}, and c_{44}, which can be computed by expanding the internal energy per unit volume as a Taylor series in elastic strain, see e.g. [38]. By applying different elastic strains, the elastic constants were determined from a polynomial fit of the ground state energy for each of the 16 χ structures in the sublattice model. The elastic constants of the χ-phase as function of Re content were calculated as [26]:

$$c_{ij}(x_{Re}) = \sum_{k,l,m,n=W,Re} y_k^A y_l^B y_m^C y_n^D c_{ij}(k,l,m,n), \tag{8}$$

where c_{ij} are either c_{11}, c_{12}, or c_{44}.

For polycrystalline materials, the Voigt and Reuss averages give the upper and lower boundaries for the bulk, K, and shear, G, moduli. In a tetragonal material, such as the σ-phase, the Voigt and Reuss averages are given as:

$$K_V = \frac{1}{9}(2c_{11} + 2c_{12} + c_{33} + 4c_{13}), \tag{9}$$

$$K_R = (2s_{11} + 2s_{12} + s_{33} + 4s_{13})^{-1}, \tag{10}$$

$$G_V = \frac{1}{15}[2c_{11} + c_{33} - (c_{12} + 2c_{13}) + 3(2c_{44} + c_{66})], \tag{11}$$

$$G_R = \frac{15}{4[2(s_{11} - s_{13}) + s_{33} - s_{12}] + 3(2s_{44} + s_{66})}, \tag{12}$$

where s_{ij} are elements of the compliance tensor. For the special case of cubic materials, such as the χ-phase, the following substitutions can be made in the equations above: $c_{12} = c_{13}$, $c_{11} = c_{33}$, $c_{44} = c_{66}$, $s_{12} = s_{13}$, $s_{11} = s_{33}$, and $s_{44} = s_{66}$.

The Hill average corresponds to the mean of the Voigt and Reuss averages [39]:

$$K_H = (K_V + K_R)/2 \tag{13}$$

$$G_H = (G_V + G_R)/2, \tag{14}$$

which were calculated from the computed elastic constants. Poisson's ratio can be calculated using K_H and G_H [40]:

$$\nu = \frac{3K_H - 2G_H}{6K_H + 2G_H}. \tag{15}$$

According to Griffith's theory of brittle fracture [29], the critical stress intensity factor, K_{IG}, at which a crack starts to grow under mode I loading and plane strain conditions is given by Sih and Liebowitz [41], Möller and Bitzek [42]

$$K_{IG} = \sqrt{\frac{G_I}{B}}, \tag{16}$$

where G_I is the energy release rate, which corresponds to the energy required to cleave the bulk crystal, while B is the appropriate crystal orientation dependent compliance constant [41]. For anisotropic materials under plane strain conditions, B can be expressed as [43]

$$B = \sqrt{\frac{b_{11}b_{22}}{2}\left(\sqrt{\frac{b_{22}}{b_{11}}} + \frac{2b_{12} + b_{66}}{2b_{22}}\right)}. \tag{17}$$

The plane strain moduli b_{ij} in the orientation of interest are defined as [41]

$$\begin{aligned} b_{11} &= \frac{s_{11}s_{33} - s_{13}^2}{s_{33}}, \quad b_{22} = \frac{s_{22}s_{33} - s_{23}^2}{s_{33}},\\ b_{12} &= \frac{s_{12}s_{33} - s_{13}s_{23}}{s_{33}}, \quad b_{66} = \frac{s_{66}s_{33} - s_{26}^2}{s_{33}}. \end{aligned} \tag{18}$$

To compute the energy release rate, G_I, associated with a cleavage plane, a supercell with a vacuum interface was utilized. The lattice was oriented such that the newly formed free surfaces were exposed, after which the atoms underwent full coordinate relaxation. A vacuum interface of 10 Å was adopted, which ensured that no interaction between the free surfaces occurred. The height of the slab was chosen based on a convergence study, where a height of minimum 13 Å was found sufficient to yield well-converged results. Once the energy release rate for all the structures in the sublattice model were obtained, G_I as function of the Re content was calculated analogously to the unstable stacking fault energies using y_c^s as weights (see Eq. (7)).

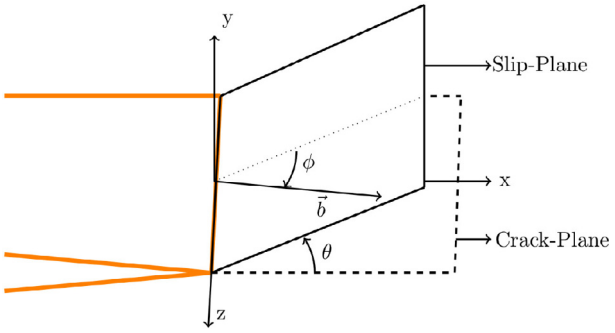

Fig. 2. Crack plane and slip system with slip direction $\vec{b}$ defined by angles θ and ϕ.

Rice's theory suggests that the critical stress intensity factor K_{IE} at which a dislocation is nucleated at the crack-tip under mode I loading and plane strain conditions, is given by Rice [30], Rice et al. [44]

$$K_{IE} = \sqrt{\frac{G_{IE}}{B}}, \tag{19}$$

with $G_{IE} = 8\frac{1+(1-\nu)\tan^2\phi}{(1+\cos\theta)\sin^2\theta}\gamma_{us}$ where ν is the Poisson's ratio as calculated by Eq. (15), γ_{us} is the unstable stacking fault energy, and the angles θ and ϕ are shown in Fig. 2.

2.4. Numerical details

For the DFT calculations, the Vienna *Ab initio* Simulation Package (VASP 5.4) was used [45,46]. We used the built-in standard projector augmented wave (PAW) pseudopotentials for W and Re [47,48] within the generalized gradient approximation based on the Perdew-Burke-Ernzerhof exchange-correlation [49]. To determine the cut-off energy, convergence tests for the σ- and χ-phases were performed, which revealed that a cut-off energy of 500 eV was sufficient for convergence for both phases. The Methfessel-Paxton method [50] for smearing with a width of 0.3 eV was applied.

The Monkhorst-Pack scheme [51] was used to generate a Γ-centered k-point grid. For the σ unit cell, a grid of $6\times6\times11$ k-points and for the χ unit cell, a grid of $6\times6\times6$ k-points were adopted. For supercells containing multiple unit cells, the k-point grid was adjusted to match the aforementioned k-point densities in reciprocal space.

The conjugate gradient method was used for ionic relaxation with a force convergence criterion of 0.01 eV/Å, except for the energy release rate calculations where an energy convergence criterion of 0.1 meV was used.

3. Results

3.1. Site occupation in σ and χ

In agreement with previous DFT works [26,28], the structures of lowest formation enthalpy in the sublattice model are, for the σ-phase, when Re atoms occupy Wyckoff sites A and D (33.3% Re) and, for the χ-phase, when Re atoms occupy Wyckoff sites C and D (82.8% Re). The two structures are entries No. 9 and No. 13 in Table A.1 in Appendix A, respectively.

Figure 3 shows the optimal Re occupation at each of the Wyckoff sites (y_{Re}) for different global Re concentrations of σ and χ. Our DFT result for the σ-phase is in good agreement with experimental data from Berne et al. [24]. For the χ-phase, experimental data were not available for comparison, but the preference of Re for the Wyckoff sites C and D, which are low coordinated sites, concur with other DFT works [25].

3.2. Close-packed planes and energy release rate

Table 1 presents the close-packed plane in the σ- and χ-phase, according to Eq. (5). The calculations were done for the sublattice structures of the lowest formation enthalpy, but the ordering

Table 1
The miller indices (hkl), the structure factor F_{hkl} (unitless), the spacing between planes d_{hkl} in units (Å) and the area-per-atom A_{hkl} in units (Å^2/atom) of the close-packed planes of σ and χ. Entries marked with † are determined visually.

σ				χ			
(hkl)	$\lvert F_{hkl}\rvert$	d_{hkl}	A_{hkl}	(hkl)	$\lvert F_{hkl}\rvert$	d_{hkl}	A_{hkl}
(004)	30.00	1.26	12.55	(114)	26.82	2.32	15.29
(140)	15.32	2.35	13.15	(330)	22.71	2.32	18.05
(002)	14.00	2.52	13.45	(004)	17.72	2.46	21.80
(330)	14.98	2.29	13.83	(550)	30.68	1.39	22.27
(110)	-	6.90	8.64†	(110)	-	6.80	9.35†

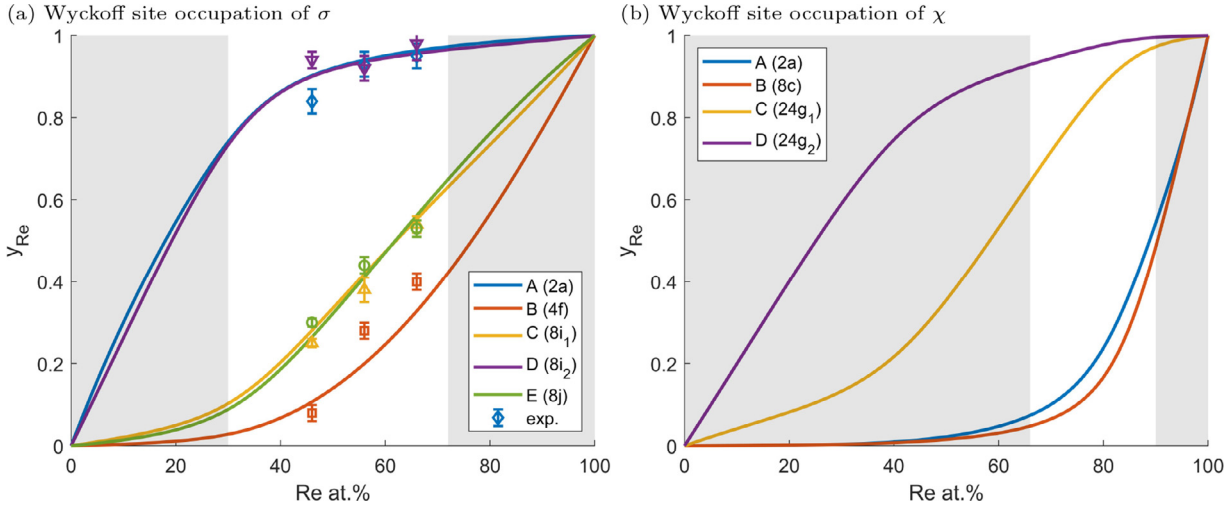

Fig. 3. Wyckoff site occupation of (a) the σ- and (b) χ-phases according to the sublattice model at T =1500 K. The Re concentrations at which the phases are thermodynamically stable according to the phase diagram [33] are indicated with white background. The Wyckoff sites are color coded with the same colors shown in the unit cells (see Fig. 1). Experimental results are from Berne et al. [24].

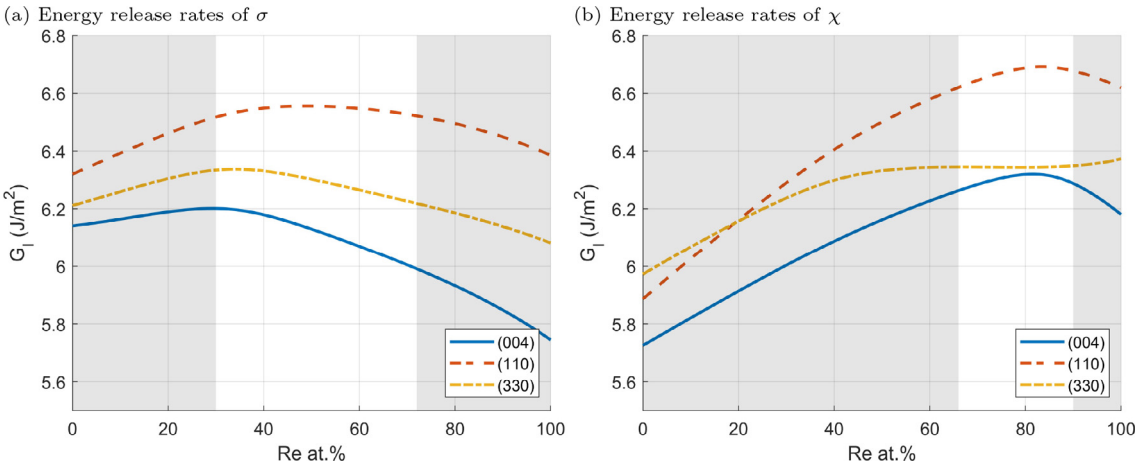

Fig. 4. Brittle energy release rates of selected cleavage planes of the (a) σ- and (b) χ- phase as a function of Re concentration. The Re concentrations at which the phases are thermodynamically stable according to the phase diagram [33] are indicated with white background.

of close-packing is applicable for all the structures since there is only little change in the internal coordinates. Several different surface terminations of each plane were probed to identify the ones with the lowest energy. The atomically flat {110}-planes were not predicted by Eq. (5) to be close-packed, but were included in our study because visual inspection of the planes indicated a low A_{hkl}. For the σ-phase, we considered the following planes: (004), (330), and (110). The (002) plane was omitted since it produced surface terminations and a GSFE profile identical to the (004) plane. The (140) plane yields a large supercell, which made it unfeasible to investigate this plane by means of DFT due to significant computational costs. For the χ-phase the (330), (004), and (110) planes were considered. While the (114) plane was predicted to have the lowest area-per-atom, it was unfeasible to investigate by means of DFT, due to its very large supercell. The (550) plane produces surfaces and GSFE identical to the (330) plane and was therefore not considered.

Figure 4 shows the brittle energy release rate, G_I, of the σ- and χ-phases for the selected close-packed planes. The energy release rate of the structures in the sublattice model are listed in Table A.2 in Appendix A. For the σ-phase, the (004) cleavage plane has the lowest G_I value. Within the phase stability range, the maximal value is 6.20 J/m^2 at 30 at.% Re and it decreases by 3% to its minimal value of 6.00 J/m^2 at 72 at.% Re. The energy release energies of the (330) and the (110) planes remain fairly constant within the phase stability range; their minimal values are 6.22 J/m^2 at 72 at.% Re and 6.52 J/m^2 at 30 at.% Re respectively. For the χ-phase, the (004) cleavage plane has the lowest G_I value. Within the stable Re concentration range, its minimal value is 6.26 J/m^2 at 66 at.% Re. The minimal G_I value of the (110) plane is 6.34 J/m^2 also located at 66 at.% Re. The value of G_I of the (330) plane remains approximately constant with a minimal value of 6.34 J/m^2 at 80 at.% Re.

3.3. Generalized stacking fault energies

The GSFE surfaces of the selected close-packed planes of the σ-phase are shown in the left column of Fig. 5. The grid indicates DFT data points, from which 2-d spline interpolation has been used to produce the GSFE surface. The density of data points is chosen so that four data points form the corners of a rectangle with an area of roughly 1 Å^2. After several tests, this density of grid points was found sufficient to yield well-converged GSFE surfaces.

For the (004) plane, shearing along ⟨100⟩ directions by a distance corresponding to the lattice vector a_0 produces the unstable stacking fault energy of $\gamma_{us} = 3.51\,\text{J/m}^2$, as indicated by the black dashed line in Fig. 5(a) and (b). There is a stable stacking fault of energy $\gamma_{ss} = 1.82\,\text{J/m}^2$ located at $(\frac{1}{2}[100], \frac{1}{8}[010])$, which can be reached without increasing γ_{us} by shearing in directions ⟨410⟩ as shown by the red line in Fig. 5(a) and (b). This suggests a possibility of dislocation dissociation into partial dislocations. For comparison, the energy curves of two additional σ structures of different Re concentrations (structures No. 17 and No. 23 in Table A.1 in Appendix A) are shown in Fig. 5(b). It can be seen that while the general features are preserved, the stable and unstable stacking fault energies are reduced.

For the GSFE landscape of the (330) plane, shown in Fig. 5(c) and (d), the shearing path of least resistance is in the [001]-direction by a distance of the lattice vector c_0. The energy barrier of this path is shown in Fig. 5(d) by the black dashed line. The unstable stacking fault energy is located at $\frac{1}{2}[001]$ and is found to be 2.44 J/m^2. Furthermore, from Fig. 5(d) it can be seen that there is a stable stacking fault located at $(\frac{1}{10}[1\bar{1}0], \frac{1}{2}[001])$ that can be reached by shearing in the $[1\bar{1}5]$ direction, as indicated by the red line in Fig. 5(c). The energy associated with the stable stacking fault is found to be 2.19 J/m^2.

For the (110) plane the unstable stacking fault energy of $\gamma_{us} = 2.70\,\text{J/m}^2$ is obtained by shearing along [001], see Fig. 5(e) and (f). Unlike the (330) plane, shearing along direction $[1\bar{1}5]$ (red line) does not lead to a lower stacking fault energy, meaning there is no stable stacking fault located at $(\frac{1}{10}[1\bar{1}0], \frac{1}{2}[001])$ for the (110) plane.

In Fig. 6 the GSFE of χ is shown for the three selected close-packed surfaces. The data for the (004) slip plane is shown in Fig. 6(a) and (b). Shearing along the ⟨010⟩ directions (black dashed line) results in an energy barrier height of 3.29 J/m^2. The barrier height can be reduced by dislocation dissociation into the ⟨540⟩ directions (red line) resulting in an unstable stacking fault energy of $\gamma_{us} = 2.96\,\text{J/m}^2$.

The energy landscape associated with shearing of the (330) plane is shown in Fig. 6(c) and (d). Shearing along the $[1\bar{1}1]$ direction, produces the lowest energy barrier. Interestingly, at the center of the GSFE surface, the resulting stacking fault energy is zero. Between the center point and the corners, there are three shallow ripples. The highest peak of these ripples is the unstable stacking fault energy: $\gamma_{us} = 2.27\,\text{J/m}^2$. Also shown in the figures is the alternative shearing path, $[2\bar{2}7]$, which reaches a stable stacking fault of $\gamma_{ss} = 1.28\,\text{J/m}^2$, however, this path is energetically unfavorable compared to $[1\bar{1}1]$, since the maximum energy barrier is higher: 2.50 J/m^2.

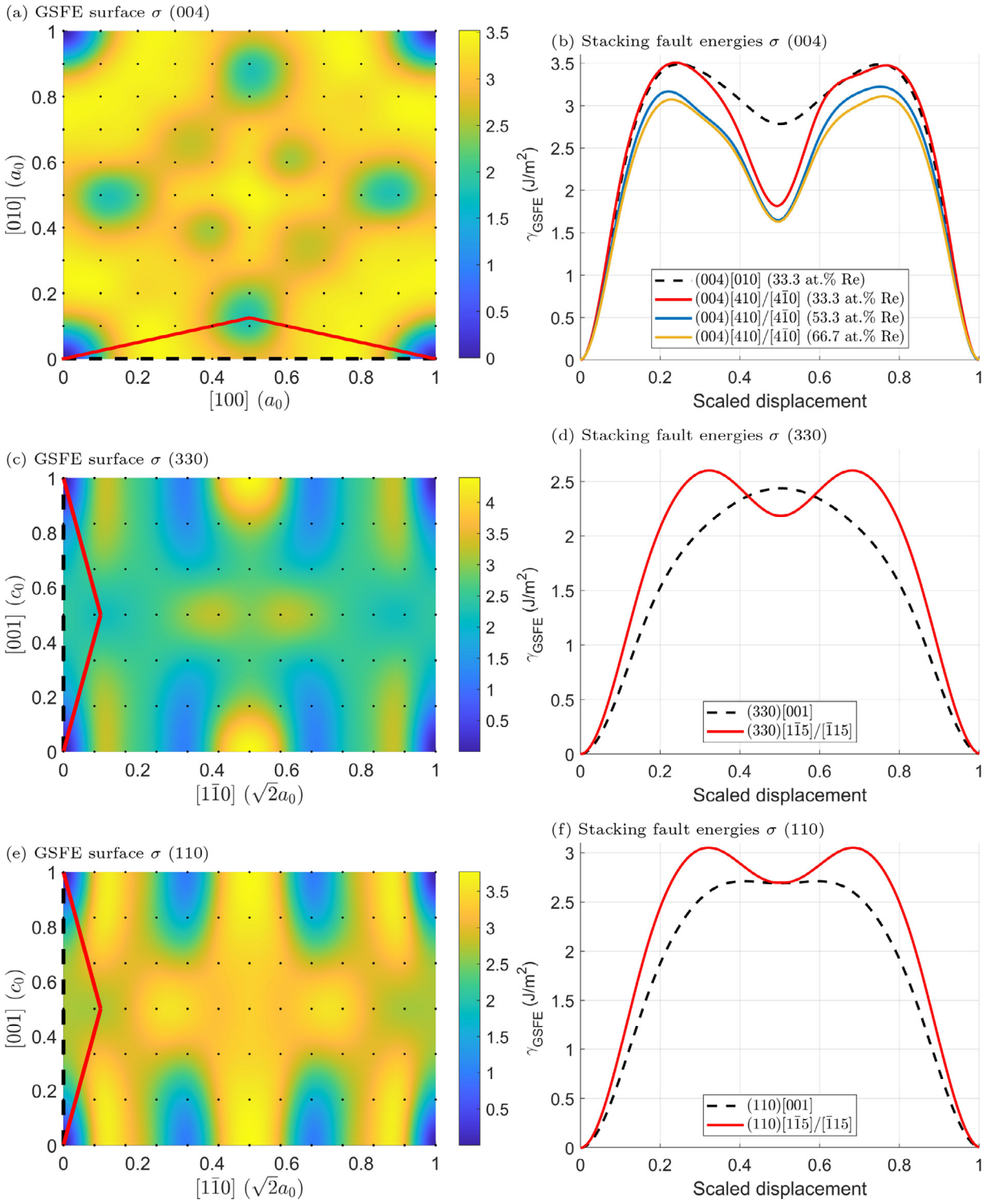

Fig. 5. Left column (a), (c) and (e): GSFE surfaces of various planes of the σ-phase (structure No. 9 in Table A.1 in Appendix A). Black dots are DFT data points, a 2D spline-fit is used for interpolation. The colored lines mark possible low-barrier paths for shearing. Right column (b), (d), and (f): The γ_{GSFE} of the shearing paths are shown.

For the (110) plane, the path [1$\bar{1}$3] leads to the lowest unstable stacking fault energy of $\gamma_{us} = 3.26\,\mathrm{J/m^2}$ and a stable stacking fault energy of $\gamma_{ss} = 1.81\,\mathrm{J/m^2}$, see Fig. 6(e) and (f). Similar to the (330) plane, shearing along [1$\bar{1}$1] will lead to zero stacking fault energy at the center but is surrounded by high energy barriers corresponding to $3.93\,\mathrm{J/m^2}$.

In Fig. 7(a), the unstable stacking fault energies of the three slip systems investigated in the σ-phase are shown as a function of Re content. In Table A.2, these energies are listed for the structures in the sublattice model for each slip system. The (330)[001] system has the lowest unstable stacking fault energy, which indicates that it is the preferred slip system for the σ-phase. Within the stable Re concentration range, γ^{σ}_{us}(330)[001] reduces by 15% from $2.30\,\mathrm{J/m^2}$ at 30 at.% Re to its minimum value of $1.95\,\mathrm{J/m^2}$ at 70 at.%. The (110)[001] slip system has the second lowest unstable stacking fault energy that remains almost constant within the

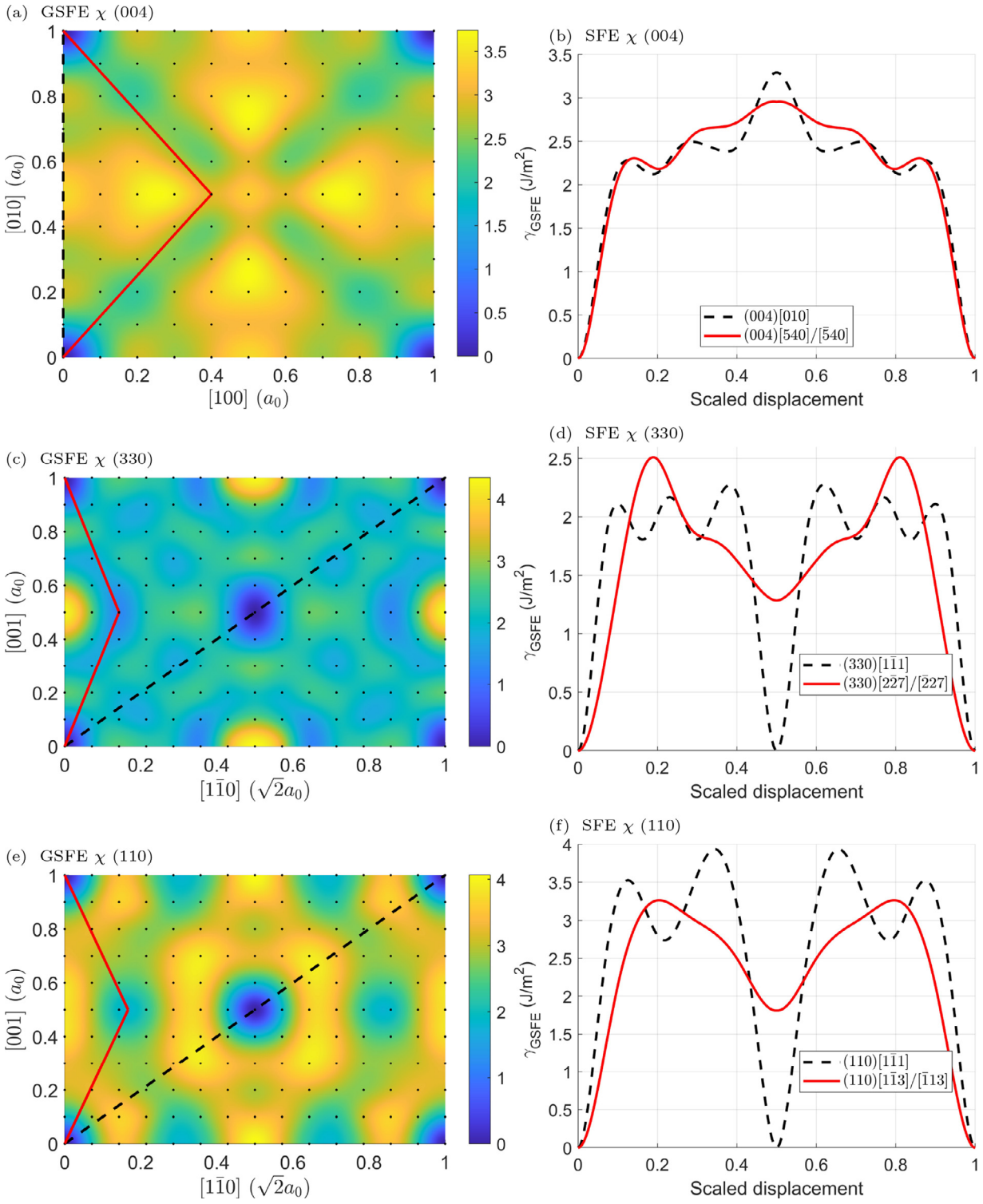

Fig. 6. Left column (a), (c), and (e): GSFE surfaces of various planes of the χ-phase (structure No. 13 in Table A.1 in Appendix A). Black dots are DFT data points, a 2D spline-fit is used for interpolation. The colored lines mark possible paths for shearing. Right column (b), (d), and (f): The γ_{GSFE} of the shearing paths are shown.

phase stability range with a minimum value of 2.67 J/m^2 at 30 at.% Re. For γ^{σ}_{us}(004)[410] we see a reduction of 9% from 3.42 J/m^2 at 30 at.% Re to 3.11 J/m^2 at 72 at.% Re.

The unstable stacking fault energies of the selected slip systems in the χ-phase are shown in Fig. 7(b). The (330)[1$\bar{1}$1] system of χ exhibits the lowest γ_{us} that, in the stable Re concentration range, decreases by 8% with increasing Re content from 2.38 J/m^2 at 66 at.% Re to 2.20 J/m^2 at 90 at.% Re. In contrast, γ^{χ}_{us}(110)[001] and γ^{χ}_{us}(004)[540] show insignificant change within the phase stability range; their minimum values of 2.89 J/m^2 and 3.18 J/m^2 are found at 66 at.% Re and 90 at.% Re respectively.

3.4. Elastic properties

Figure 8 shows the elastic properties of both phases as a function of the Re content. The elastic properties of the structures

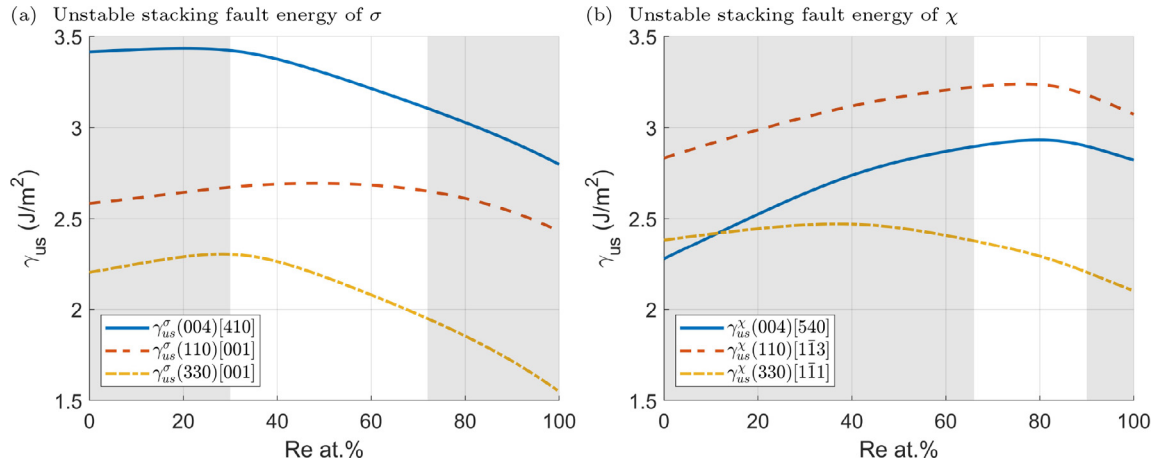

Fig. 7. Unstable stacking fault energies of (a) σ and (b) χ as a function of Re concentration as calculated by Eq. (7). The Re concentrations at which the phases are thermodynamically stable according to Massalski et al. [33] are indicated with white background.

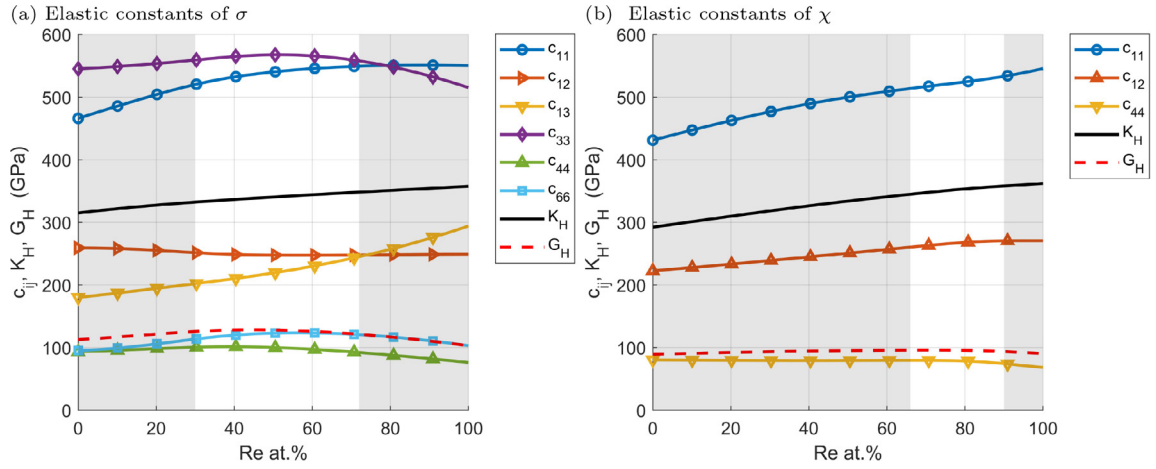

Fig. 8. Elastic constants of (a) σ and (b) χ as a function of global rhenium content according Eq. (8). The Re concentrations at which the phases are stable according to phase diagram [33] are shown in white background.

in the sublattice model are listed in Table A.3 in Appendix A. In Fig. 8(a) the six elastic constants of the tetragonal σ-phase are shown as well as the Hill average of the bulk, K_H, and shear, G_H, moduli. The elastic data for the σ-phase is from [26], but we emphasize that we have confirmed its accuracy herein. Within the phase stability range, there is little change in the elastic constants with respect to the Re content, except for c_{13} which increases by 21% from 202 GPa at 30 at.% Re to 245 GPa at 72 at.% Re. In the same concentration range, K_H increases by 4.8% from 332 GPa to 348 GPa, while G_H decreases from 126 GPa to 121 GPa with a peak value of 128 GPa at 44 at.% Re.

In Fig. 8(b) the three elastic constants, bulk and shear moduli of the χ-phase are shown. Similar to the σ-phase, the Re concentration has little effect on the elastic constants within the thermodynamically stable Re concentration range. The parameter c_{11}, cf. Fig. 8(b), experiences the largest change with a 4% increase from 513 GPa at 66 at.% Re to 533 GPa at 90 at.% Re. The bulk modulus K_H increases by 4% from 345 GPa to 358 GPa, while G_H remains roughly constant; its minimum value is 93 GPa at 90 at.% Re.

3.5. Fracture toughness

The critical stress intensity factors K_{IG} and K_{IE} can be estimated using Eqs. (16) and (19). Since mode I fracture and slip usually occurs on close-packed planes, we limit ourselves to the previously selected planes as the crack and slip planes. In the case of K_{IE}, the Burgers vector will point in the direction leading to the lowest energy barrier, i.e. the unstable stacking fault energy.

For the σ-phase, when either {110} or {330} act as a crack plane, the crack can either grow through brittle fracture along the crack plane or the crack tip can blunt by emitting a dislocation onto slip planes of type {004} with a Burgers vector in direction $\langle 100\rangle$, which corresponds to $\theta = 90^\circ$ and $\phi = 45^\circ$ in Fig. 2. In the case of crack planes of type {004}, both the {110} and {330} planes can act as slip planes, with the Burgers vector along $\langle 001\rangle$ ($\theta = 90^\circ$ and $\phi = 0^\circ$). However, the {330} plane is preferred since it has a lower unstable stacking fault energy (see Fig. 7) resulting in a lower value of K_{IE}.

Likewise for the χ-phase, when either {110} or {330} act as a crack plane, the crack tip can blunt by emitting a dislocation onto {004} slip planes with a Burgers vector in direction $\langle 540\rangle$ ($\theta = 90^\circ$ and $\phi = 6.3^\circ$). For crack planes of type {004}, plasticity may ensue by emission of a dislocation onto {330} slip planes with the Burgers vector $\langle 1\bar{1}1\rangle$ ($\theta = 90^\circ$ and $\phi = 45^\circ$).

In Fig. 9 K_{IG} and K_{IE} are plotted for the σ- and χ-phases. It can be seen that, within the phase stability range, K_{IE} shows a relatively stronger dependency on the Re content and crack system due to its dependency on γ_{us}, whereas K_{IG} shows weak dependency on the Re content. In general, the value of K_{IE} is about 1.6-2.5 times higher than that of K_{IG}. Within the phase stability range, K_{IG} varies between 1.67–1.80 MPa·m$^{1/2}$ for σ and 1.55–1.62 MPa·m$^{1/2}$ for χ, while K_{IE} varies between 2.75–4.68 MPa·m$^{1/2}$

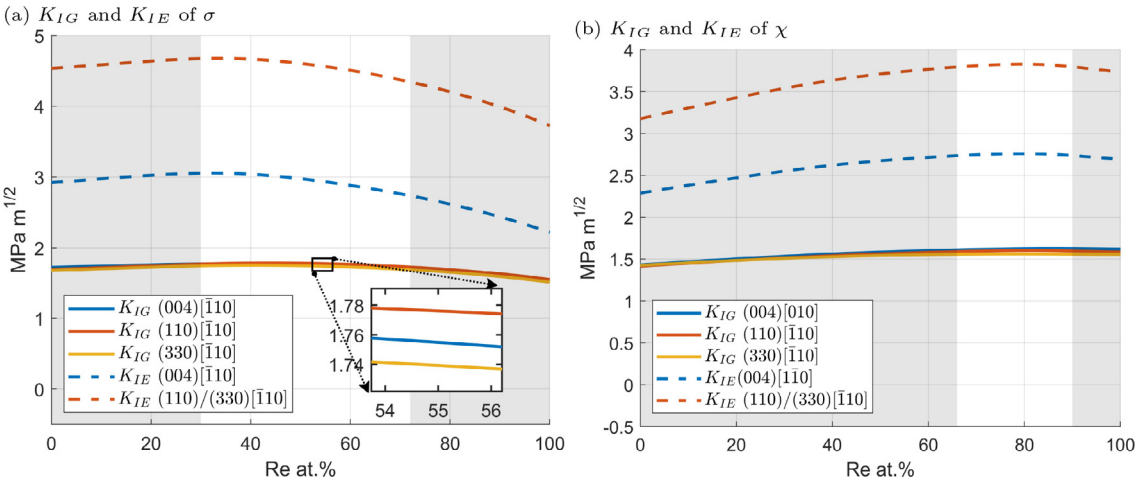

Fig. 9. Griffith's and Rice's critical stress intensity factors for the (a) σ- and (b) χ-phases. The Re concentrations at which the phases are thermodynamically stable according to the phase diagram [33] are indicated with white background.

for σ and 2.74–3.83 MPa·m$^{1/2}$ for χ depending on the Re concentration and crack system.

4. Discussion

The close-packed planes were determined by adopting Eq. (5), which provided a straightforward means of assessing the packing-density of crystal planes. This method tends to preferentially select highly corrugated planes, such as the (140) plane in σ and the (114) plane in χ, which could easily be overlooked by visual inspection due to their high level of corrugation. However, the atomically flat (110) plane was not predicted to be close-packed, while visual inspection found it to be the most close-packed plane in both phases.

Within the stable Re concentration range, the (004) plane of both the σ and χ-phase had the lowest energy release rate. However, the energy release rate of the probed planes remains fairly similar in value with roughly an 8% difference between the highest and lowest energy for the σ-phase and a 6% difference for the χ-phase. Furthermore, the energy release rate showed a weak dependency on the Re content: within the stable Re concentration range, the change was just a few percent.

As the σ- and χ-phases have complex crystal structures it is not surprising that the GSFE-landscapes have high complexity as well. We have attempted to identify reasonable slip systems that yield the lowest possible energy barriers. The lower value of γ_{us}(330)[001] as compared to the other slip systems investigated, indicates that this slip system is preferred for both phases. Within the stable Re concentration range, γ_{us}(330)[001] reduces with increasing Re content, resulting in a minimal value of 1.95 J/m^2 for σ and 2.20 J/m^2 for χ. In BCC W (see Table 2) unstable stacking fault energies of 1.8 J/m^2 and 1.9 J/m^2 were computed for the (110) and (112) planes, respectively [52]. The higher unstable stacking fault energies of the σ- and χ-phases indicate an increased resistance to dislocation nucleation and slip.

Table 2 also presents the bulk and shear moduli of W as calculated by means of DFT, which are in good agreement with experimental values, presented in Table 3. From the same table, it can be seen that increasing the Re content in W causes only a slight increase in the elastic moduli. Comparing the DFT results of W with the σ- and χ-phases shows a 9% and 12% higher bulk modulus for σ and χ, respectively, and a 22% and 42% lower shear modulus. For the σ- and χ-phases, a tendency of increasing bulk modulus with increasing Re content was observed, while the shear modulus showed a weak dependency with only a few percent change in value. The lower value of G_H of the precipitates compared to the W matrix, suggests precipitation hardening due to the shear modulus misfit [54]. Another possible mechanism for precipitation hardening is the pinning of dislocations by impenetrable precipitates, which has been indicated by molecular dynamics simulations [55].

Because experimental data on the fracture toughness of W-Re σ and χ are not available, we estimate them based on Griffith and Rice theories. While K_{IG} has a very weak dependency on the Re content, K_{IE}, which depends on the unstable stacking fault energy, shows a stronger dependency on Re content. We note a reduction of up to 10% with increasing Re content. Despite this reduction, the value of K_{IE} is roughly 1.6-2.5 times higher than K_{IG}. This would imply that brittle fracture behavior is preferred in both phases.

Table 2
Table of BCC W properties based DFT calculations from the supplementary material of [52].

W, DFT [52]			
Elastic properties (GPa)			
C_{11}	544	K_H	313
C_{12}	198	G_H	159
C_{44}	149		
Unstable stacking fault energies (J/m^2)			
γ^{us}_{110}	1.80		
γ^{us}_{112}	1.90		
Critical stress intensity (MPa · m$^{1/2}$)			
Crack system		K_{IG}	K_{IE}
(001)[0$\bar{1}$0]		2.08	2.96
(001)[1$\bar{1}$0]		2.06	2.54
(110)[$\bar{1}$10]		1.84	2.41
(110)[001]		1.82	3.36

Table 3
Table of experimental values of W and W-Re elastic properties (GPa) [53].

W, Exp. [53]			
Elastic property	W 298K	W-3at.%Re 80K	W-10at.%Re 80K
C_{11}	529	541	531
C_{12}	209	213	218
C_{44}	162	163	171
K_H	316	322	322
G_H	161	163	165

Listed in Table 2 are estimates of K_{IG} and K_{IE} for selected crack systems in BCC W. Comparison shows that the value of K_{IG} for the σ- and χ-phases are 2%-13% and 11%-23% lower than BCC W depending on the crack system. The lower value of K_{IG} suggests a reduced resistance to brittle fracture for the precipitates. As for Rice theory, the values for K_{IE} in W are in the same range of values estimated for the σ- and χ-phases. However, it should be noted that due to underlying simplifications, Griffith theory tends to underestimate [56] and Rice theory tends to overestimate [57] the true value of the critical stress intensity factor.

5. Summary and conclusions

An *ab-initio* investigation of mechanical and fracture-related properties of the σ- and χ-phases was performed. The following parameters were determined: the elastic constants of χ, the brittle energy release rates and generalized stacking fault energies for both phases, as well as the unstable stacking fault energies. These parameters were used to evaluate the fracture toughness based on Griffith and Rice theories. Furthermore, to account for the non-stoichiometry of the phases, a sublattice model was adopted to determine the dependency of the aforementioned parameters on the Re content.

The σ- and χ-phases were found to be more compliant than BCC W, with a 22% and 42% decrease in the Hill averages of the shear modulus. This would indicate that hardening due to shear modulus misfit between σ and χ precipitates and a W (W-Re) matrix could be a contributing factor to the experimentally observed hardening.

Griffith's and Rice's theories were used to determine the fracture toughness and the following conclusions were drawn:

- The value of K_{IE} is 1.6-2.5 times higher than K_{IG} for the σ- and χ-phases. This would suggest brittle fracture preference in both phases.
- Compared to DFT data of BCC W, depending on the crack system a 2%-13% reduction in K_{IG} for σ and an 11%-23% reduction for χ was found, indicating a reduced resistance to brittle fracture.

Within the phase stability range, it was discovered that *increasing* the Re content leads to the following trends:

- Energy release rates, elastic constants, and shear modulus vary only by a few percent. The bulk modulus increased by less than 8% for the σ-phase and by 4% for the χ-phase.
- The unstable stacking fault energies showed a stronger dependency on Re content, with up to a 15% reduction of $\gamma_{us}(330)[001]$ for the σ-phase and an 8% reduction of $\gamma_{us}(330)[1\bar{1}1]$ for the χ-phase.
- The parameter K_{IG} showed insignificant dependency on Re content, while K_{IE} decreased by a few percent.

The weak dependency on Re content indicates that, within the phase stability range, the elemental composition of the phases has little influence on the fracture-related properties and it is rather the structure of the crystal that dictates the behavior.

Declaration of Competing Interest

The authors declare that they have no known competing financial interests or personal relationships that could have appeared to influence the work reported in this paper.

CRediT authorship contribution statement

Anders Vesti: Conceptualization, Methodology, Investigation, Formal analysis, Writing – original draft, Writing – review & editing. **Praveenkumar Hiremath:** Methodology, Writing – original draft, Writing – review & editing. **Solveig Melin:** Writing – review & editing, Supervision, Funding acquisition. **Pär A.T. Olsson:** Conceptualization, Methodology, Writing – review & editing, Supervision, Funding acquisition.

Data availability

The data required to reproduce these findings will be provided by the corresponding author upon reasonable request. The data needed to reproduce many of the results are given in Appendix A.

Acknowledgments

The authors gratefully acknowledge funding from the Swedish Research Council (grant agreements No. 2016-04162 and No. 2018-04348). The computations were enabled by resources provided by the Swedish National Infrastructure for Computing (SNIC) at the National Supercomputer Centre (NSC), Linköping University.

Appendix A. DFT data of the σ- and χ-phases

Table A.1 lists the basic parameters of each of the sublattice structures of the σ- and χ-phases. The numbering (No.) is used to distinguish between the structures. Table A.2 lists the energy release rate and stacking fault energies, while Table A.3 contains the elastic properties of the σ- and χ-phases. The unit cell volumes,

Table A.1
Data for the σ- and χ-phases. The sublattice structure number, No., the elements of the Wyckoff sites $ABCD(E)$, the rhenium concentration, x_{Re}, the formation enthalpy H_f in units (eV/at.), and volume per atom V_0 (Å^3/at).

σ					χ				
No.	*ABCDE*	x_{Re}	H_f	V_0	No.	*ABCD*	x_{Re}	H_f	V_0
1	WWWWW	0.000	0.173	16.24	1	WWWW	0.000	0.289	16.37
2	ReWWWW	0.067	0.141	16.15	2	ReWWW	0.035	0.299	16.34
3	WReWWW	0.133	0.189	16.09	3	WReWW	0.138	0.315	16.34
4	ReReWWW	0.200	0.162	16.01	4	ReReWW	0.172	0.329	16.19
5	WWWWRe	0.267	0.162	15.92	5	WWReW	0.414	0.137	15.83
6	WWWReW	0.267	0.054	15.88	6	WWWRe	0.414	0.058	15.82
7	WWReWW	0.267	0.143	15.98	7	ReWReW	0.448	0.151	15.79
8	ReWWWRe	0.333	0.130	15.85	8	ReWWRe	0.448	0.064	15.79
9	ReWWReW	0.333	0.026	15.80	9	WReReW	0.552	0.199	15.71
10	ReWReWW	0.333	0.111	15.85	10	WReWRe	0.552	0.092	15.70
11	WReWWRe	0.400	0.177	15.79	11	ReReReW	0.586	0.216	15.67
12	WReWReW	0.400	0.071	15.75	12	ReReWRe	0.586	0.105	15.67
13	WReReWW	0.400	0.167	15.78	13	WWReRe	0.828	-0.006	15.34
14	ReReWWRe	0.467	0.153	15.71	14	ReWReRe	0.862	0.002	15.31

(*continued on next page*)

Table A.1 (*continued*)

σ					χ				
No.	*ABCDE*	x_{Re}	H_f	V_0	No.	*ABCD*	x_{Re}	H_f	V_0
15	ReReWReW	0.467	0.032	15.66	15	WReReRe	0.966	0.036	15.22
16	ReReReWW	0.467	0.139	15.70	16	ReReReRe	1.000	0.049	15.18
17	WWWReRe	0.533	0.055	15.60					
18	WWReWRe	0.533	0.136	15.65					
19	WWReReW	0.533	0.059	15.59					
20	ReWWReRe	0.600	0.036	15.52					
21	ReWReWRe	0.600	0.108	15.58					
22	ReWReReW	0.600	0.034	15.51					
23	WReWReRe	0.667	0.077	15.47					
24	WReReWRe	0.667	0.166	15.52					
25	WReReRew	0.667	0.087	15.46					
26	ReReWReRe	0.733	0.055	15.40					
27	ReReReWRe	0.733	0.138	15.45					
28	ReReReReW	0.733	0.066	15.38					
29	WWReReRe	0.800	0.081	15.33					
30	ReWReReRe	0.867	0.066	15.26					
31	WReReReRe	0.933	0.114	15.22					
32	ReReReReRe	1.000	0.095	15.14					

Table A.2
The brittle energy release rate and unstable stacking fault energies associated with the (hkl) plane of the σ- and χ-phases in units of (J/m^2). The number, No., refers to the structures listed in Table A.1.

	σ						χ					
No.	$G_I^{(004)}$	$G_I^{(110)}$	$G_I^{(330)}$	$\gamma^{us}_{(004)}$	$\gamma^{us}_{(110)}$	$\gamma^{us}_{(330)}$	$G_I^{(004)}$	$G_I^{(110)}$	$G_I^{(330)}$	$\gamma^{us}_{(004)}$	$\gamma^{us}_{(110)}$	$\gamma^{us}_{(330)}$
1	6.14	6.32	6.21	3.41	2.58	2.20	5.73	5.89	5.97	2.28	2.83	2.38
2	6.17	6.43	6.31	3.42	2.63	2.24	5.70	5.78	5.99	2.24	2.78	2.38
3	5.86	6.12	6.10	3.24	2.21	2.05	5.46	5.72	5.88	2.08	2.62	2.19
4	5.89	6.23	6.21	3.22	2.26	2.10	5.40	5.60	5.86	2.02	2.55	2.18
5	6.07	6.07	6.18	3.03	2.48	2.09	6.11	6.44	6.27	2.66	3.25	2.43
6	6.22	6.47	6.31	3.49	2.63	2.39	6.13	6.48	6.40	2.84	3.16	2.56
7	5.78	6.40	5.87	3.31	2.78	1.48	6.04	6.31	6.31	2.61	3.19	2.43
8	6.12	6.22	6.31	3.02	2.54	2.16	6.10	6.39	6.43	2.82	3.14	2.55
9	6.29	6.59	6.43	3.49	2.70	2.44	5.68	6.11	5.98	2.36	2.86	2.11
10	5.96	6.62	6.10	3.47	2.97	1.68	5.90	6.30	6.30	2.63	2.92	2.29
11	5.85	5.90	6.06	2.49	2.02	1.82	5.59	5.99	5.99	2.31	2.78	2.10
12	5.99	6.32	6.20	3.34	2.31	2.27	5.86	6.20	6.32	2.60	2.88	2.27
13	5.53	6.20	5.86	3.08	2.38	1.39	6.39	6.76	6.33	2.99	2.29	2.29
14	5.87	6.02	6.18	2.77	2.09	1.88	6.37	6.71	6.38	2.98	3.27	2.29
15	5.95	6.39	6.24	3.23	2.27	2.23	6.24	6.67	6.30	2.82	3.09	2.09
16	5.52	6.26	5.91	2.99	2.34	1.35	6.18	6.62	6.37	2.82	3.07	2.10
17	6.23	6.34	6.30	3.15	2.66	2.43						
18	6.41	6.72	6.43	3.73	3.54	2.18						
19	5.95	6.70	6.08	3.39	2.90	1.74						
20	6.23	6.43	6.39	3.11	2.67	2.46						
21	6.07	6.51	6.21	3.21	3.07	1.71						
22	6.00	6.80	6.17	3.35	2.90	1.75						
23	5.96	6.15	6.12	2.93	2.23	2.15						
24	5.54	5.98	5.83	2.67	2.27	1.20						
25	6.00	6.76	6.28	3.52	2.84	2.00						
26	6.08	6.33	6.32	3.04	2.39	2.36						
27	5.94	6.43	6.28	3.15	2.80	1.75						
28	6.08	6.91	6.40	3.57	2.92	2.08						
29	5.89	6.43	5.99	2.91	2.76	1.58						
30	5.88	6.51	6.07	2.88	2.76	1.62						
31	5.63	6.21	5.90	2.68	2.29	1.37						
32	5.74	6.39	6.08	2.80	2.43	1.55						

Table A.3
Table of the elastic properties of the σ- and χ-phases. The elastic constants c_{ij}, the Hill averages of the bulk, K_H, and shear G_H moduli are listed in units of GPa. Data for the σ-phase is from Bonny et al. [26]. The number, No., refers to the structures listed in Table A.1.

	σ								χ				
No.	c_{11}	c_{12}	c_{13}	c_{33}	c_{44}	c_{66}	K_H	G_H	c_{11}	c_{12}	c_{44}	K_H	G_H
1	466	259	180	545	93	95	315	113	431	223	80	292	89
2	487	258	180	549	93	93	318	114	430	223	78	292	87
3	464	270	189	526	86	82	320	104	440	226	67	297	80
4	474	272	191	528	87	83	324	106	438	228	63	298	78
5	481	258	198	563	95	88	324	115	518	227	82	324	103
6	525	261	203	553	102	107	338	126	496	246	78	330	94
7	483	267	201	526	79	95	327	103	514	231	82	325	102

(*continued on next page*)

Table A.3 (*continued*)

No.	σ								χ				
	c_{11}	c_{12}	c_{13}	c_{33}	c_{44}	c_{66}	K_H	G_H	c_{11}	c_{12}	c_{44}	K_H	G_H
8	497	252	200	567	95	95	326	118	497	246	75	330	92
9	533	246	205	562	105	122	334	131	484	249	68	327	85
10	502	261	203	524	84	100	330	109	494	254	61	334	80
11	490	262	203	552	87	75	328	108	480	252	66	328	82
12	519	258	207	561	101	102	336	124	491	257	57	335	77
13	484	261	208	511	77	89	325	100	526	272	81	356	97
14	498	260	213	547	91	87	332	112	527	272	81	357	97
15	535	255	206	573	108	120	340	133	539	269	66	359	88
16	501	263	212	529	85	96	333	100	545	270	68	362	91
17	540	239	216	587	105	123	337	133					
18	510	240	227	526	75	108	328	104					
19	549	245	221	550	93	128	341	124					
20	548	242	222	605	110	127	343	137					
21	578	303	262	525	78	114	383	108					
22	561	244	226	574	97	142	346	130					
23	546	252	227	588	102	111	347	129					
24	518	232	275	510	66	101	336	94					
25	551	241	229	550	85	89	341	114					
26	549	257	229	600	112	112	350	136					
27	525	244	265	485	75	107	340	101					
28	557	256	231	568	92	135	351	124					
29	554	230	264	520	74	128	343	107					
30	554	241	271	531	75	120	350	107					
31	546	235	285	491	70	105	347	99					
32	550	249	294	515	76	103	357	103					

elastic constants and elastic moduli of the σ-phase are adopted from [26].

References

[1] J. Linke, J. Du, T. Loewenhoff, G. Pintsuk, B. Spilker, I. Steudel, M. Wirtz, Challenges for plasma-facing components in nuclear fusion, Matter Rad. Extremes 4 (2019) 056201.

[2] H. Bolt, V. Barabash, W. Krauss, J. Linke, R. Neu, S. Suzuki, N. Yoshida, A.U. Team, Materials for the plasma-facing components of fusion reactors, J. Nucl. Mater. 329 (2004) 66–73.

[3] N. Noda, V. Philipps, R. Neu, A review of recent experiments on W and high Z materials as plasma-facing components in magnetic fusion devices, J. Nucl. Mater. 241 (1997) 227–243.

[4] S.J. Zinkle, Fusion materials science: overview of challenges and recent progress, Phys. Plasmas 12 (5) (2005) 058101.

[5] Y. Qian, M.R. Gilbert, L. Dezerald, D. Cereceda, Using first-principles calculations to predict the mechanical properties of transmuting tungsten under first wall fusion power-plant conditions, J. Phys. Condens. Matter 33 (34) (2021) 345901.

[6] V. Philipps, Tungsten as material for plasma-facing components in fusion devices, J. Nucl. Mater. 415 (1) (2011) S2–S9.

[7] R.G. Abernethy, Predicting the performance of tungsten in a fusion environment: a literature review, Mater. Sci. Technol. 33 (2017) 388–399.

[8] S. Krat, Y. Gasparyan, A. Pisarev, I. Bykov, M. Mayer, G. de Saint Aubin, M. Balden, C.P. Lungu, A. Widdowson, Erosion at the inner wall of JET during the discharge campaign 2011–2012 in comparison with previous campaigns, J. Nucl. Mater. 456 (2015) 106–110.

[9] T. Hirai, S. Panayotis, V. Barabash, C. Amzallag, F. Escourbiac, A. Durocher, M. Merola, J. Linke, T. Loewenhoff, G. Pintsuk, et al., Use of tungsten material for the ITER divertor, Nucl. Mater. Energy 9 (2016) 616–622.

[10] R.A. Pitts, X. Bonnin, F. Escourbiac, H. Frerichs, J.P. Gunn, T. Hirai, A.S. Kukushkin, E. Kaveeva, M.A. Miller, D. Moulton, et al., Physics basis for the first ITER tungsten divertor, Nucl. Mater. Energy 20 (2019) 100696.

[11] M.R. Gilbert, S.L. Dudarev, S. Zheng, L.W. Packer, J.C. Sublet, An integrated model for materials in a fusion power plant: transmutation, gas production, and helium embrittlement under neutron irradiation, Nucl. Fusion 52 (2012) 083019.

[12] R.G. Abernethy, J.S.K.L. Gibson, A. Giannattasio, J.D. Murphy, O. Wouters, S. Bradnam, L.W. Packer, M.R. Gilbert, M. Klimenkov, M. Rieth, H.C. Schneider, C.D. Hardie, S.G. Roberts, D.E.J. Armstrong, Effects of neutron irradiation on the brittle to ductile transition in single crystal tungsten, J. Nucl. Mater. 527 (2019) 151799.

[13] G.A. Cottrell, R. Pampin, N.P. Taylor, Transmutation and phase stability of tungsten armor in fusion power plants, Fusion Sci. Technol. 50 (2006) 89–98.

[14] Y. Nemoto, A. Hasegawa, M. Satou, K. Abe, Microstructural development of neutron irradiated W-Re alloys, J. Nucl. Mater. 283–287 (2000) 1144–1147.

[15] T. Tanno, M. Fukuda, S. Nogami, A. Hasegawa, Microstructure development in neutron irradiated tungsten alloys, Mater. Trans. 52 (2011) 1447–1451.

[16] M. Fukuda, T. Tanno, S. Nogami, A. Hasegawa, Effects of Re content and fabrication process on microstructural changes and hardening in neutron irradiated tungsten, Mater. Trans. 53 (2012) 2145–2150.

[17] M. Dürrschnabel, M. Klimenkov, U. Jäntsch, M. Rieth, H.C. Schneider, D. Terentyev, New insights into microstructure of neutron-irradiated tungsten, Sci. Rep. 11 (7572) (2021).

[18] M.J. Lloyd, A.J. London, J. Haley, M.R. Gilbert, C. Becquart, C. Domain, E. Martinez, M. Moody, P. Bagot, D. Nguyen-Manh, D. Armstrong, Interaction of transmutation products with precipitates, dislocations and grain boundaries in neutron irradiated W, Materialia (2022) 101370.

[19] T. Suzudo, M. Yamaguchi, A. Hasegawa, Stability and mobility of rhenium and osmium in tungsten: first principles study, Modell. Simul. Mater. Sci. Eng. 22 (2014) 075006.

[20] T. Suzudo, M. Yamaguchi, A. Hasegawa, Migration of rhenium and osmium interstitials in tungsten, J. Nucl. Mater. 467 (2015) 418–423.

[21] L. Gharaee, P. Erhart, A first-principles investigation of interstitial defects in dilute tungsten alloys, J. Nucl. Mater. 467 (2015) 448–456.

[22] L. Gharaee, J. Marian, P. Erhart, The role of interstitial binding in radiation induced segregation in W-Re alloys, J. Appl. Phys. 120 (2) (2016) 025901.

[23] C.-H. Huang, L. Gharaee, Y. Zhao, P. Erhart, J. Marian, Mechanism of nucleation and incipient growth of Re clusters in irradiated W-Re alloys from kinetic Monte Carlo simulations, Phys. Rev. B 96 (9) (2017) 094108.

[24] C. Berne, M. Sluiter, Y. Kawazoe, T. Hansen, A. Pasturel, Site occupancy in the Re-W sigma phase, Phys. Rev. B 64 (2001) 144103.

[25] J.C. Crivello, J.M. Joubert, First principles calculations of the σ and χ phases in the Mo-Re and W-Re systems, J. Phys. Condens. Matter 22 (2009) 035402.

[26] G. Bonny, A. Bakaev, D. Terentyev, Y.A. Mastrikov, Elastic properties of the sigma W-Re phase: a first principles investigation, Scr. Mater. 128 (2017) 45–48.

[27] G. Bonny, A. Bakaev, D. Terentyev, Y.A. Mastrikov, Interatomic potential to study plastic deformation in tungsten-rhenium alloys, J. Appl. Phys. 121 (2017) 165107.

[28] W. Setyawan, N. Gao, R.J. Kurtz, A tungsten-rhenium interatomic potential for point defect studies, J. Appl. Phys. 123 (2018) 205102.

[29] A.A. Griffith, VI. The phenomena of rupture and flow in solids, Philos. Trans. R. Soc.London Ser. A 221 (582–593) (1921) 163–198.

[30] J.R. Rice, Dislocation nucleation from a crack tip: an analysis based on the Peierls concept, J. Mech. Phys. Solids 40 (2) (1992) 239–271.

[31] K. Momma, F. Izumi, VESTA 3 for three-dimensional visualization of crystal, volumetric and morphology data, J. Appl. Crystallogr. 44 (6) (2011) 1272–1276.

[32] J.-M. Joubert, J.-C. Crivello, Non-stoichiometry and Calphad modeling of Frank-Kasper phases, Appl. Sci. 2 (3) (2012) 669–681.

[33] T.B. Massalski, H. Okamoto, P. Subramanian, L. Kacprzak, W.W. Scott, Binary alloy phase diagrams, Vol. 1, American Society for Metals, Metals Park, OH, 1986.

[34] J.-M. Joubert, Crystal chemistry and Calphad modeling of the σ phase, Prog. Mater. Sci. 53 (3) (2008) 528–583.

[35] J.-M. Joubert, M. Phejar, Crystal chemistry and Calphad modelling of the χ phase, Prog. Mater. Sci. 54 (7) (2009) 945–980.

[36] J.-C. Crivello, A. Breidi, J.-M. Joubert, χ and σ phases in binary rhenium–transition metal systems: a systematic first-principles investigation, Inorg. Chem. 52 (7) (2013) 3674–3686.
[37] P.M. Kelly, H.-P. Ren, D. Qiu, M.X. Zhang, Identifying close-packed planes in complex crystal structures, Acta Mater. 58 (2010) 3091–3095.
[38] P.A.T. Olsson, A.R. Massih, J. Blomqvist, A.-M.A. Holston, C. Bjerkén, Ab initio thermodynamics of zirconium hydrides and deuterides, Comput. Mater. Sci 86 (2014) 211–222.
[39] R. Hill, The elastic behaviour of a crystalline aggregate, Proc. Phys. Soc. London Sect. A 65 (5) (1952) 349–354.
[40] N. Zotov, A. Ludwig, First-principles calculations of the elastic constants of Fe–Pt alloys, Intermetallics 16 (1) (2008) 113–118.
[41] G.C. Sih, H. Liebowitz, Fracture: an advanced treatise, Math. Fundam. 2 (1968) 68–188.
[42] J.J. Möller, E. Bitzek, Fracture toughness and bond trapping of grain boundary cracks, Acta Mater. 73 (2014) 1–11.
[43] J.J. Möller, E. Bitzek, Comparative study of embedded atom potentials for atomistic simulations of fracture in α-iron, Modell. Simul. Mater. Sci. Eng. 22 (4) (2014) 045002.
[44] J.R. Rice, et al., Mathematical analysis in the mechanics of fracture, Fracture 2 (1968) 191–311.
[45] G. Kresse, J. Hafner, Ab initio molecular dynamics for liquid metals, Phys. Rev. B 47 (1) (1993) 558.
[46] G. Kresse, J. Furthmüller, Efficiency of ab-initio total energy calculations for metals and semiconductors using a plane-wave basis set, Comput. Mater. Sci 6 (1) (1996) 15–50.
[47] G. Kresse, D. Joubert, From ultrasoft pseudopotentials to the projector augmented-wave method, Phys. Rev. B 59 (1999) 1758–1775.
[48] P.E. Blöchl, Projector augmented-wave method, Phys. Rev. B 50 (1994) 17953–17979.
[49] J.P. Perdew, K. Burke, M. Ernzerhof, Generalized gradient approximation made simple, Phys. Rev. Lett. 77 (1996) 3865–3868.
[50] M. Methfessel, A.T. Paxton, High-precision sampling for Brillouin-zone integration in metals, Phys. Rev. B 40 (6) (1989) 3616.
[51] H.J. Monkhorst, J.D. Pack, Special points for Brillouin-zone integrations, Phys. Rev. B 13 (12) (1976) 5188.
[52] P. Hiremath, S. Melin, E. Bitzek, P.A.T. Olsson, Effects of interatomic potential on fracture behaviour in single-and bicrystalline tungsten, Comput. Mater. Sci 207 (2022) 111283.
[53] R.A. Ayres, G.W. Shannette, D.F. Stein, Elastic constants of Tungsten-Rhenium alloys from 77 to 298 K, J. Appl. Phys. 46 (4) (1975) 1526–1530.
[54] K.C. Russell, L.M. Brown, A dispersion strengthening model based on differing elastic moduli applied to the iron-copper system, Acta Metall. 20 (7) (1972) 969–974.
[55] G. Bonny, A. Bakaev, D. Terentyev, Assessment of hardening due to non-coherent precipitates in tungsten-rhenium alloys at the atomic scale, Sci. Rep. 9 (2019) 2045–2322.
[56] A. Mattoni, L. Colombo, F. Cleri, Atomic scale origin of crack resistance in brittle fracture, Phys. Rev. Lett. 95 (11) (2005) 115501.
[57] Y. Sun, G.E. Beltz, J.R. Rice, Estimates from atomic models of tension-shear coupling in dislocation nucleation from a crack tip, Mater. Sci. Eng. A 170 (1–2) (1993) 67–85.